

修 士 論 文

題 目

Broadband frequency
entangled photon
generation using silicon
nitride ring cavities

指導教員

竹内 繁樹 教授

京都大学大学院工学研究科 電子工学専攻

氏 名

殷 政浩

令和2年2月1日

Broadband frequency entangled photon generation using silicon nitride ring cavities

Zhengkao Yin

Abstract

Lorem ipsum dolor sit amet, consectetur adipiscing elit. Ut purus elit, vestibulum ut, placerat ac, adipiscing vitae, felis. Curabitur dictum gravida mauris. Nam arcu libero, nonummy eget, consectetur id, vulputate a, magna. Donec vehicula augue eu neque. Pellentesque habitant morbi tristique senectus et netus et malesuada fames ac turpis egestas. Mauris ut leo. Cras viverra metus rhoncus sem. Nulla et lectus vestibulum urna fringilla ultrices. Phasellus eu tellus sit amet tortor gravida placerat. Integer sapien est, iaculis in, pretium quis, viverra ac, nunc. Praesent eget sem vel leo ultrices bibendum. Aenean faucibus. Morbi dolor nulla, malesuada eu, pulvinar at, mollis ac, nulla. Curabitur auctor semper nulla. Donec varius orci eget risus. Duis nibh mi, congue eu, accumsan eleifend, sagittis quis, diam. Duis eget orci sit amet orci dignissim rutrum.

Contents

1	Introduction	1
1.1	Background	1
1.2	Objective	2
1.3	Outline	2
2	Principal theory	3
2.1	Guided-wave optics	3
2.1.1	Waveguide modes	4
2.1.2	Dispersion relation	5
2.2	Ring resonators	6
2.2.1	Coupling condition	6
2.2.2	Spectrum characteristics	7
2.3	Thrid-order nonlinear optics	8
3	Phase match condition for spontaneous four wave mixing in a ring cavity	12
3.1	Chromatic dispersion	13
3.2	Dispersion compensation	14
3.3	Dispersion engineering using slot structure	15
3.4	Effects of mode crossing	16
4	Device fabrication of silicon nitride ring resonators	18
4.1	Subtractive fabrication process	18
4.1.1	Film deposition	19
4.1.2	Material properties	20
4.1.3	Patterning	20
4.1.4	ICP etching	21
4.1.5	Top-cladding and annealing	21
4.1.6	Edge coupling and chip dicing	22
4.2	Fabless samples via foundries	22
4.2.1	Ligentec technique	23

4.2.2 NTT-AT technique	23
5 Dispersion evaluation from transmission spectroscopy	24
5.1 Methods	24
5.2 Setups	24
5.3 Results	24
5.3.1 Device transmission	24
5.3.2 Dispersion	24
6 Broadband Photon pair generation	25
6.1 Joint spectrum intensity	25
6.2 Coincidence counts vs. pump	25
7 Towards intermodal and intramodal photon pair	26
7.1 Spontaneous four wave mixing	26
7.2 Stimulated four wave mixing	26
8 Summary	27
Acknowledgements	28
References	29
Appendix A Dispersion simulation	44
Appendix B Layout design	45
Appendix C Process	46

Chapter 1

Introduction

The flying qubit—photon—featuring the advantages of long coherent time and multiple degrees of freedom (DoF), is a promising candidate in quantum computation and quantum communication. However, in the term of DoF, much of research up to now focuses on the photon polarization and path entanglement realization, very little attention has been paid to the role of frequency entanglement, which is continuous and infinite in hilbert space.

Furthermore, the previous research shows that frequency entangled photon pairs can be exploited not only in wavelength division multiplexing quantum key distribution [1] but also transferring quantum information in future quantum networks [2]. Besides, in recent applications of quantum metrology, quantum optical coherent tomography (QOCT), the broadband frequency entanglement [3] is also required.

1.1 BACKGROUND

Compared with crystal experiments, a chip-scale photon source has the advantages of scalability and robustness. A conventional material candidate is silicon on insulator (SOI), since it is CMOS-compatible and supplied by a lot of wafer manufacturers. However, suffering from two photon absorption and stimulated Raman scattering, silicon is no able to generate broadband frequency conversion. Since that, silicon nitride, which is transparent from visible to near infrared range, is preferred to perform broadband frequency entanglement. A recent record is single pair from visible to telecom band [4].

1.2 OBJECTIVE

In the platform of silicon nitride, we utilize the third-order optical nonlinearity and confine the light in the sub-micron scale—optical waveguides. To enhance the nonlinear interaction, we define the ring resonator and couple the light inside along with a bus waveguide. The broadband property is ensured by carefully optimizing the device geometry to achieve a broadband phase matching condition. All the photon pair generation events are detected by single photon detectors and verified by the coincident counting.

In this dissertation, the terms 'broadband photon pair' is used to describe that pairs are generated in different frequency pairs simultaneously and but entangled only in the single mode pair.

1.3 OUTLINE

The following chapters are sequentially divided in different topics.

Chapter 2

Principal theory

The way how light travels in a chip-scale is remarkably different the way in free-space. In the sub-micron scale, the electromagnetic wave can only propagate in a few cycles due to the constraint of material boundaries. However, since atoms and molecules are much smaller, the refractive index is not changed, as well as the reflection, interference and diffraction.

Based on these facts, in order to perform quantum optics experiments *at the bottom*, first, we shall confine the light propagation in a specific waveguide. On the other hand, thanks to modern laser technology, nonlinear optics is involved and give birth to optical frequency conversion. To enhance these nonlinear optical phenomena, we adopt the cavity structure and achieve sizable control.

In this chapter, we briefly introduce the guided wave theory and then move the cavity structure, ring resonators. Next, the nonlinear optics, in particular third-order nonlinear processes, is discussed in the following section. Although the quantum nature of photon pair generation distinct from the classical theory, all the physics mentioned above are necessary to analyse our essential research object, the silicon nitride ring resonators.

2.1 GUIDED-WAVE OPTICS

In an ideal optical waveguide, the core layer and the cladding layer are usually composed of two different materials, where the refractive index is larger in the core. As an analogue of optical fibers, only in the higher index region can the light propagate, and meanwhile dissipate in a wavelength scale in the lower index region.

Usually, we assume the core and the cladding layer are made of nonmagnetic (magnetic permeability $\mu = \mu_0$) and dielectric material (conductivity $\sigma = 0$). Furthermore, we neglect the nonlinear response of the polarization of electric field ($\mathbf{P} \simeq \varepsilon_0 \chi \mathbf{E}$).

Since the waveguide in numerous research objects, is deposited or sputtered using chemical or physical methods, the uneven density in the waveguide layer can not be negligible. Hence, the propagation equation derived from Maxwell's equation is

$$(\nabla_{\perp}^2 + k^2 n^2 - \beta^2) \mathbf{E} = -(\nabla_{\perp} + i\beta \hat{\mathbf{z}})(\mathbf{E}_{\perp} \cdot \nabla_{\perp} \ln n^2) \quad (2.1)$$

where \perp denotes the transverse component, $\nabla_{\perp}^2 = \nabla_x^2 + \nabla_y^2$. And k, n, β are the wave vector in vacuum, refractive index and propagation constant, respectively. While, with the negligible film anisotropy, Equation 2.1 can be approximated into

$$(\nabla_{\perp}^2 + k^2 n^2 - \beta^2) \mathbf{E} = 0 \quad (2.2)$$

This is the normal *Helmholtz equation*, indicating the relation between propagation constant β and material refractive index, i.e. *chromatic dispersion*.

Next, the boundary conditions determining the solution to Eqn. 2.2, arise from the Maxwell's equations as well.

$$\begin{aligned} \hat{\mathbf{n}} \cdot (\mathbf{E}_a - \mathbf{E}_b) &= 0 \\ \hat{\mathbf{n}} \times (\mathbf{H}_a - \mathbf{H}_b) &= 0 \end{aligned}$$

which is the continuity condition of both electric and magnetic field at all dielectric material interfaces. Here, $\hat{\mathbf{n}}$ is the normal direction at the material boundary and the subscript a, b denote different regions.

2.1.1 Waveguide modes

In the case of channel waveguides, the index discontinuity from both vertical and horizontal sides can be decomposed into two sets of independent and complete conditions, i.e. the horizontal boundary condition and vertical boundary condition, with the discontinuity on the waveguide corners neglected. In other words, approximately the equation has two independent particular solutions, which is the mathematical origin of *transverse electric* (TE) modes and *transverse magnetic* (TM) modes.

Hence, we can study the eigenequation by selecting only one set of boundary condition, as used in the *the effective index method*. For example, in a planar waveguide shown in Figure 2.1, $d^2/dy^2 = 0$ ¹, the TE mode features $E_x = 0$ and consider only y -component,

$$\frac{d^2 E_y}{dx^2} + (k^2 n^2 - \beta^2) E_y = 0 \quad (2.3)$$

and E_y is continuous at $x = \pm d/2$, where d is the thickness of core layer.

For the region $|x| > d/2$, the light evanesces at x -direction at rate κ and in contrast, in the region of core layer, the light performs like stationary wave, denoting with k_x . By substituting these conditions, phase continuity is achieved between two interface

$$2k_x d = m\pi + 2 \arctan(\kappa/k_x) \quad (2.4)$$

where m is the index of stationary wave. The second term can be treated as the Goos-Hänchen phase shift. Overall, the waveguide modes characterize that the phase shall maintain itself with an $m\pi$ shift along with the shift at the boundaries.

In the case of TM modes, the eigen equation is

$$2k_x d = m\pi + 2 \arctan(\delta\kappa/k_x) \quad (2.5)$$

where $\delta = n_a/n_b$ is the index ratio and only differs from Equation 2.4 with this parameter. conclusively, the less is δ parameter, the propagation constant of TE and TM modes are closer.

2.1.2 Dispersion relation

Based on Equation 2.4 and Equation 2.5, k_x can be solved and then utilized to calculate propagation constant β , since $n_a^2 k^2 = k_\perp^2 + \beta^2$. In the case of channel waveguides, the TE and TM solutions are both necessary. Therefore, propagation constants β can be expressed as the product of free space wave vector k and the *effective index* n_{eff}

$$\beta = n_{\text{eff}} k = n_{\text{eff}}(\lambda) \frac{2\pi}{\lambda} = n_{\text{eff}}(\omega) \frac{\omega}{c} \quad (2.6)$$

¹Since the planar waveguide is infinite at the y -direction, thus the solution is identical in arbitrary xz -plane, which means no gradient along x -axis.

along with the differential form

$$\frac{d\beta}{dk} = n_{\text{eff}} + k \frac{dn_{\text{eff}}}{dk} = n_{\text{eff}} - \lambda \frac{dn_{\text{eff}}}{d\lambda} \equiv n_g \quad (2.7)$$

$$\frac{d\omega}{d\beta} = c \frac{dk}{d\beta} = \frac{c}{n_g} \equiv v_g \quad (2.8)$$

which defines the group index n_g and group velocity v_g .

This formula linking $\beta-k$ or $\beta-\omega$ is named as dispersion relation, which gives the physics that light with different color propagates at different *speed*. Furthermore, Equation 2.4 and Equation 2.5 also indicate that the dispersion relation intrinsically depends on waveguide geometry.

2.2 RING RESONATORS

The ring resonators comprise of a bus waveguide and a ring waveguide, are usually demonstrated as optical filters or modulators at a wide range of platforms. The working principle of ring resonator can be derived completely [5] as an analogue to Fabry-Pérot etalon, based on the coupling mode theory.

In the model illustrated in Figure 2.2, the self-coupling coefficient τ and the cross-coupling coefficient κ can be evaluated analytically or using numerical simulation. Assuming the coupling only occur at the very close area, τ, κ are the power splitting ratios of the coupler and satisfy $\tau^2 + \kappa^2 = 1$ if the coupling section is lossless. a is the single-pass amplitude transmission, including both propagation loss in the ring and loss in the couplers.

The transmission rate of a all-pass type ring cavity takes the form of

$$T = \frac{I_{\text{pass}}}{I_{\text{input}}} = \frac{a^2 - 2a\tau \cos \phi + \tau^2}{1 - 2a\tau \cos \phi + a^2\tau^2} \quad (2.9)$$

where $\phi = \beta L$ is the phase shift in a single round trip.

2.2.1 Coupling condition

By plotting the function in Figure 2.3, we can see, the extinction ratio of absorption peak is defined by the self-coupling coefficient τ and the single-pass amplitude transmission a due to device geometric differences, like the gap between the bus waveguide and the

ring cavity. Namely, a and τ both determine the coupling condition, which can be categorized in three cases

- **weak coupling** $a > \tau$. The loss inside the ring is larger than the power coupled from bus waveguides.
- **critical coupling** $a = \tau$. The loss and self-coupling are in balance. The optical power restored in the resonator achieve the minimum.
- **over coupling or strong coupling** $a < \tau$. The coupling is too strong for the light to dissipate in a single round trip.

Previous work [6] proposed a method to evaluate the coupling condition above using the experimentally measured device transmission. Considering the loss in the coupler, bent segment of ring and higher mode perturbation, usually the critical coupling varies from modes and the cross section of waveguides [7].

2.2.2 Spectrum characteristics

Meanwhile, the minimum of transmission rate T can be achieved periodically as $\phi = 2m\pi$, which defines the resonance of ring resonators. Therefore, the resonance condition is derived as

$$\beta L = 2m\pi \quad (2.10)$$

where m is the mode index. Specifically, the propagation constant β , shall be an integral times of a quasi wave vector $2\pi/L$. With this condition, the free spectral range (FSR) of wavelength and frequency are obtained

$$\Delta\lambda_{\text{FSR}} \approx \frac{\lambda_{\text{res}}^2}{n_g L} \quad (2.11)$$

$$\Delta\omega_{\text{FSR}} \approx \frac{2\pi c}{n_g L} \quad (2.12)$$

In both wavelength and frequency domain, FSR determines the spacing of neighbouring resonant peak. This is a significant factor when the ring resonators are designed.

Furthermore, from Equation 2.9, the full width at half maximum (FWHM) of the resonance spectrum is derived as $\delta\lambda$

$$\delta\phi = \frac{2(1 - a\tau)}{\sqrt{\tau a}} \quad (2.13)$$

Likely, since the phase ϕ is related with the wave vector k in Equation 2.7. Substituting $\delta\phi = Ln_g\delta k$, the half width of wavelength is

$$\delta\lambda = \frac{d\lambda}{dk}\delta k = \frac{\lambda_{\text{res}}^2}{2\pi Ln_g} \frac{2(1-a\tau)}{\sqrt{\tau a}} \quad (2.14)$$

the same, at the frequency domain

$$\delta\omega = \frac{d\omega}{dk}\delta k = \frac{c}{Ln_g} \frac{2(1-a\tau)}{\sqrt{\tau a}} \quad (2.15)$$

Note in Equation 2.11 Equation 2.12 Equation 2.14 and Equation 2.15, the group index n_g is explicit instead of the effective index n_{eff} because both free spectral range and full width depend on the differential form, Equation 2.7.

And the finesse F of the resonator is defined

$$F \equiv \frac{2\pi}{\delta\phi} = \frac{\pi\sqrt{\tau a}}{2(1-a\tau)} \quad (2.16)$$

Finally, we define the quality factor, a measure of the sharpness of the resonance relative to its central frequency.

$$Q = \frac{\lambda_{\text{res}}}{\delta\lambda} = \frac{\pi Ln_g\sqrt{\tau a}}{\lambda_{\text{res}}(1-a\tau)} \quad (2.17)$$

Usually, the Q -factor can be decomposed into two parts by formula $Q^{-1} = Q_i^{-1} + Q_l^{-1}$. And Q_i, Q_l are intrinsic Q -factor and loaded Q -factor, referring to the loss inside the ring waveguide and at the coupler, respectively. The physical meaning of the finesse and Q -factor relates to the number of round-trips before being lost to internal loss and the bus waveguides when the power is depleted to $1/e$ of its initial value.

2.3 THRID-ORDER NONLINEAR OPTICS

Although the nonlinear effect is ignored during the derivation of waveguide modes in Section 2.1, for numerous materials, the nonlinear response of electric field is significant even at mW level, which is easy to occur with assistance of modern lasers. The origin of nonlinear optic phenomena is similar to the movement of the object in a potential field, such as the ball-spring model.

In the nonlinear material, the atoms or molecules are driven by the external electric field, due to the around chemical bonds or molecular orientation, the displacement of atoms or molecules perform nonlinear dependence on the strength of field. In real-world materials, interaction coming arising from various frequency leads to the addition or subtraction of these frequency components. This explains the frequency conversion nature in nonlinear optics.

It is worth mentioning that not only in the bulk crystals, but also in the sub-micron scale [8], the nonlinear response is still efficient, even over a single-layer two-dimensional material.

Here, a brief theoretical derivation is elucidated and in the following part, degenerate four wave mixing is emphasized. In an isotropic nonlinear medium, assuming only instantaneous dielectric response, the relation between the polarization and the electric field is expressed by a power series in the electric field

$$\mathbf{P}(t) = \varepsilon_0(\chi^{(1)}\mathbf{E}(t) + \chi^{(2)}\mathbf{E}^2(t) + \chi^{(3)}\mathbf{E}^3(t)) = \varepsilon_0\chi^{(1)}\mathbf{E}(t) + \mathbf{P}_{\text{NL}}(t) \quad (2.18)$$

Note in Equation 2.18, the nonlinear susceptibilities $\chi^{(2)}$ and $\chi^{(3)}$ are second-rank and third-rank tensors, corresponding to the tensor product with \mathbf{E}^2 and \mathbf{E}^3 . The higher order response is neglected and sequentially, only $\chi^{(2)}$ processes and $\chi^{(3)}$ processes are to be introduced.

$\chi^{(2)}$ processes

In centrosymmetric crystals such as silicon, the second-order susceptibility term is absent. However, in other materials like lithium niobate (LiNbO_3) and aluminium nitride (AlN), the second-order non-linearity are essential to realize electro-optic modulation and second harmonic generation.

$\chi^{(3)}$ processes

Silicon and silicon nitride are both cubic crystal. Due to the third-order dependence, another factor equivalent to the optical intensity is involved, the $\chi^{(3)}$ process is also named as intensity-dependent effect or Kerr effect.

Consider three frequency components of \mathbf{E}^3 , using the complex expression of electric field

$$\mathbf{E}(\mathbf{r}, t) = \sum_{k=1}^3 \mathbf{E}_{\omega_k}(\mathbf{r}, t) = \frac{1}{2} \sum_{k=1}^3 (\mathbf{E}_{\omega_k}(\mathbf{r})e^{i\omega_k t} + c.c.) \quad (2.19)$$

Substituting into third-order term in Equation 2.18 and arranging with the same propagation direction, the third-order polarization is

$$\mathbf{P}^{(3)}(t) = \frac{3}{4}\varepsilon_0\chi^{(3)} [|\mathbf{E}_{\omega_1}|^2\mathbf{E}_{\omega_1} + \dots] \quad \text{SPM} \quad (2.20)$$

$$+ \frac{6}{4}\varepsilon_0\chi^{(3)} [(|\mathbf{E}_{\omega_2}|^2 + |\mathbf{E}_{\omega_3}|^2)\mathbf{E}_{\omega_1} + \dots] \quad \text{XPM} \quad (2.21)$$

$$+ \frac{1}{4}\varepsilon_0\chi^{(3)} [(\mathbf{E}_{\omega_1}^3 e^{i\omega_1 t} + c.c.) + \dots] \quad \text{THG} \quad (2.22)$$

$$+ \frac{3}{4}\varepsilon_0\chi^{(3)} \left[\frac{1}{2}(\mathbf{E}_{\omega_1}^2 \mathbf{E}_{\omega_2} e^{i(2\omega_1+\omega_2)t} + c.c.) + \dots \right] \quad \text{FWM} \quad (2.23)$$

$$+ \frac{3}{4}\varepsilon_0\chi^{(3)} \left[\frac{1}{2}(\mathbf{E}_{\omega_1}^2 \mathbf{E}_{\omega_2}^* e^{i(2\omega_1-\omega_2)t} + c.c.) + \dots \right] \quad \text{FWM} \quad (2.24)$$

$$+ \frac{6}{4}\varepsilon_0\chi^{(3)} \left[\frac{1}{2}(\mathbf{E}_{\omega_1} \mathbf{E}_{\omega_2} \mathbf{E}_{\omega_3} e^{i(\omega_1+\omega_2+\omega_3)t} + c.c.) + \dots \right] \quad \text{FWM} \quad (2.25)$$

$$+ \frac{6}{4}\varepsilon_0\chi^{(3)} \left[\frac{1}{2}(\mathbf{E}_{\omega_1} \mathbf{E}_{\omega_2} \mathbf{E}_{\omega_3}^* e^{i(\omega_1+\omega_2-\omega_3)t} + c.c.) + \dots \right] \quad \text{FWM} \quad (2.26)$$

In above equations, \dots stands for all possible permutation terms contributed by frequencies $\omega_1, \omega_2, \omega_3$. The abbreviation on the right side represent for

SPM, self-phase modulation

SPM adds an intensity-dependent term except the linear polarization, leading to a broadening of the pulse spectrum.

Note the $\chi^{(3)}$ is complex, thus the imaginary part may contribute to another intensity-dependent absorption mechanics, which is usually depicted in the *two-photon absorption* (TPA). The free carriers excited by TPA in further change the temporally both the absorption coefficient and the refractive index of material.

$$n = n_0 + n_2 I + i \frac{\lambda}{4\pi} (\alpha_0 + \alpha_2 I) \quad (2.27)$$

where the I is the intensity, n_2 is the Kerr coefficient and α_0, α_2 are related with TPA-induced free carrier absorption (FCA) and free carrier index (FCI) change, both interrelated with third-order susceptibility

$$n_2 = \frac{1}{c n_0^2 \varepsilon_0} \frac{3}{4} \text{Re}\{\chi^{(3)}\} \quad (2.28)$$

$$\alpha_2 = \frac{-\omega}{c^2 n_0^2 \varepsilon_0} \frac{3}{2} \text{Im}\{\chi^{(3)}\} \quad (2.29)$$

A figure of merit (FOM) is often used to compare the magnitude of Kerr coefficient n_2 with the strength of the TPA coefficient α_2

$$\text{FOM} = \frac{1}{\lambda} \frac{n_2}{\alpha_2} \quad (2.30)$$

XPM, cross-phase modulation

XPM can be seen the first signal index influenced by a second signal. And the coefficient of XPM is twice as strong as the SPM coefficient.

THG, third-harmonic generation

Like SHG, THG generated a new frequency with is one-third of input frequency.

FWM, four wave mixing

In FWM process, more than three frequencies are involved. Nevertheless, Equation 2.23 and Equation 2.24 contain two identical wave, sometime calles as degenerate four wave mixing (DFWM). And Equation 2.25 and Equation 2.26 is a truly four wave process. Similar to the relation between SPM and XPM, the non-degenerate FWM is naturally twice stronger.

Traditionally, following the terminology in laser field, in DFWM, the ω_1 square term Equation 2.24 is labeled as pump frequency, and another two frequencies are referred to signal and idler frequency.

Besides, the imaginary part of third-order susceptibility incorporate other four-wave absorption mechanics, such as *stimulated Brillouin scatter* (SBS) and *stimulated Raman scattering* (SRS), which originate from acoustic waves in crystals and vibrating molecules.

Finally, it worth mentioning that in all THG and FWM processes, different from SPM and XPM processes, phase matching condition is required due to the complex exponential factors. In this case, the phase mismatch can change the polarization rapidly and leads to periodical variation in these parametric processes.

Chapter 3

Phase match condition for spontaneous four wave mixing in a ring cavity

According to the previous chapter, in a typical nonlinear optical waveguide or silica fibers, despite the stimulated Raman and Brillouin scattering, the frequency conversion processes involve not only the self-phase modulation of pump light and cross-phase modulation of signal and idler light, but also the phase mismatch in four wave mixing propagation factor. In this case, it is necessary to study the coupled nonlinear equations involving signal, idler and pump intensity [9].

Whereas in ring resonators, whose mode linewidth (pm) is much narrower than self-phase modulation frequency broadening, the frequency broadening in single mode is negligible. Thus the phase mismatch among cavity modes becomes the critical factor of the band of four wave mixing.

This chapter first describes the major origin of phase mismatch, chromatic dispersion, and goes on to the design philosophy used in device fabrication. Besides, several topics concerning the band of phase matching are also included.

3.1 CHROMATIC DISPERSION

In a typical FWM process, both energy conservation and momentum conservation are required

$$\beta_i + \beta_s = 2\beta_p \quad (3.1)$$

$$\omega_i + \omega_s = 2\omega_p \quad (3.2)$$

where the subscripts s i p stand for signal, idler and pump light.

Meanwhile, the resonance condition Equation 2.10 leads to $\beta = m\frac{2\pi}{L}$. Thus, Equation 3.1 is equivalent to

$$m_i + m_s = 2m_p \quad (3.3)$$

We can see that *the momentum conservation agrees with mode number conservation*. That is to say, as pump light sets into resonant wavelengths, by choosing the equidistant modes relative to the pump mode, the momentum conservation can be naturally satisfied. This is the most important difference from non-resonant devices.

Therefore, we can estimate the phase mismatch only in the frequency domain. Expand the resonant frequency into Taylor series at ω_0 to the propagation constant β

$$\begin{aligned} \omega_\mu &= \omega_0 + \sum_{j=1} \frac{d^j \omega}{d\beta^j} \frac{(\beta - \beta_0)^j}{j!} \\ &= \omega_0 + \sum_{j=1} \frac{d^j \omega}{d\beta^j} \left(\frac{2\pi}{L} \right)^j \frac{\mu^j}{j!} \\ &= \omega_0 + D_1 \mu + \frac{D_2}{2!} \mu^2 + \frac{D_3}{3!} \mu^3 + \dots \end{aligned} \quad (3.4)$$

where $D_j \equiv (\frac{2\pi}{L})^j d^j \omega / d\beta^j$ are j -order mode number dispersion parameter, whose dimension are all T^{-1} and $\mu \in \mathbb{Z}$ is the relative mode number.

It is easy to know that $D_1/2\pi = v_g/L$ is the free spectral range in the frequency and indicates that the dispersion property is related with the difference of resonant frequencies.

Next, we introduce the integrated dispersion D_{int} [10] to analyze the phase mismatch

$$\begin{aligned} D_{\text{int}}(\mu) &\equiv \omega_\mu - (\omega_0 + D_1 \mu) \\ &= \frac{D_2}{2!} \mu^2 + \frac{D_3}{3!} \mu^3 + \dots \end{aligned} \quad (3.5)$$

In particular, D_{int} is the residual dispersion higher than second order. Approximately, if $D_3\mu \ll D_2$, the second-order dispersion will dominate the integrated dispersion both at signal and idler mode.

Indeed, the mode number dispersion parameter is linked with the dispersion coefficients in frequency and wavelength domain, giving such a chain rule

$$D_2 = -\frac{L}{2\pi} D_1^3 \beta_2 = \frac{L}{2\pi} \frac{\lambda^2}{2\pi c} D_1^3 D_\lambda \quad (3.6)$$

where $\beta_2 = d^2\beta/d\omega^2$ is group velocity dispersion (GVD) and $D_\lambda = -(\lambda/c) d^2n/d\lambda^2$ is the dispersion parameter.

In this method, we can analyze the phase mismatch in FWM quantitatively

$$\begin{aligned} \Delta\omega &\equiv \omega_s + \omega_i - 2\omega_p \\ &= D_{\text{int}}(\mu) + D_{\text{int}}(-\mu) \\ &= 2 \left(\frac{D_2\mu^2}{2!} + \frac{D_4\mu^4}{4!} + \frac{D_6\mu^6}{6!} + \dots \right) \end{aligned} \quad (3.7)$$

From the above derivation, the frequency mismatch $\Delta\omega$ only adds to the even terms of Taylor series in Equation 3.4. To conclude, a rough presupposition to increase the efficient phase matched band is achieving zero and flat dispersion around pump wavelengths.

3.2 DISPERSION COMPENSATION

Previously mentioned in Section 2.1, the dispersion behaviour in integrated devices is not only the intrinsic material property, but also depends on the waveguide dimension.

In other words, the phase mismatch occurs as a result of material dispersion D_M and waveguide dispersion D_W , $D_\lambda = D_M + D_W$. Here, we adopt the wavelength dispersion parameter since the wavelength domain is measurable.

Usually, the Sellmeier equation is used to fit the refractive index for a particular transparent medium based on the Lorentz-Drude mode. Luke *et al.* reported the below measured refractive index of stoichiometric Si_3N_4 film [11]

$$n_{\text{Si}_3\text{N}_4}^2 = 1 + \frac{3.0249\lambda^2}{\lambda^2 - 135.3406^2} + \frac{40314\lambda^2}{\lambda^2 - 1239842^2} \quad (3.8)$$

This Sellmeier equation is valid over the wavelength range 310–5504 nm. The result of Equation 3.8 is plotted in Figure 3.1, along with the material dispersion parameter D_M , which is calculated at the precision of nm using the second-order finite difference of refractive index. In the telecom C-band, $n=1.9963$ and $D_M = -6.57$ ps/(km nm), which suggests the material dispersion at this range is considerably small.

On the other hand, the numerical simulation is adopted to evaluate the waveguide parameter. We use commercial software *Lumerical MODE* to solve for the refractive index of fundamental TE modes. Shown in Figure 3.2, the dimension dependence of waveguide dispersion features negative values in the small waveguide size, i.e. behaving as normal dispersion at the second order. Nevertheless, as either the thickness or width of channel waveguide increases, D_W turns positive. This indicates that to achieve zero dispersion in phase match condition of four wave mixing, the normal material dispersion can be compensated with anomalous waveguide dispersion.

For example, at 1550 nm, in a 1.5- μm -wide and 0.8- μm -thick silicon nitride waveguide cladded by silica, where the refractive index is 1.48, the waveguide dispersion is 45 ps/(km nm). Substituting into the second-order dispersion chain rule in Equation 3.6, the second-order mode number dispersion parameter D_2 is about 12 kHz. It is close to zero dispersion for the pump wavelength.

3.3 DISPERSION ENGINEERING USING SLOT STRUCTURE

The slot waveguide was firstly realized by Xu *et al.* experimentally [12]. In the same group Almeida *et al.* then discussed the light enhancement and confinement caused by large discontinuity of the electric field at high-index-contrast interfaces [13]. In the recent decade, it is fully studied that such a novel waveguide can be also used to design dispersion-flattened waveguide [14–17], including the both vertical or horizontal and single or multiple slots. It is also reported a micro-ring resonators formed by a slot hybrid waveguide exhibits a flat and low anomalous dispersion [18].

In our research, the vertical slot waveguide is preferred because it is easy to realized based on the monolithic fabrication process.

We propose a double-slot silicon nitride to achieve near-zero and flat dispersion.

In a double vertical slot waveguide illustrated in Figure 3.3 , two vertical slots are fully etched and cladded with silica instead. Except the waveguide width w and thickness t , two extra parameters are defined. The position factor (pf) is the ratio of slot position to the waveguide width. And the filling factor (ff) is the ratio of slot width to the waveguide width.

To classify the modes in this slot structure, the same mode solver mention in previous section is adopted to plot the electric field intensity in Figure 3.4. An interesting finding is that differing from the simple rectangular waveguide, the mode of both quasi-TE and quasi-TM modes can be assumed as the symmetric and anti-symmetric combination of the mode field on both sides.

$$\begin{aligned} \mathbf{E}_{\text{sym}} &= \mathbf{E}_l + \mathbf{E}_r \\ \mathbf{E}_{\text{asym}} &= \mathbf{E}_l - \mathbf{E}_r \end{aligned} \tag{3.9}$$

Figure 3.5 is the z-component of the electric field of the four modes. For example, quasi-TE0 mode is even parity while quasi-TE1 mode is odd parity.

Furthermore, by optimizing the position and filling factors, the near-zero and flattened dispersion is obtained.

3.4 EFFECTS OF MODE CROSSING

In the conclusion of Section 3.2, only in the wider or thicker waveguides can the zero dispersion be compensated. However, despite the fabrication difficulty arising from thicker films, the waveguide of larger size also supports high order modes.

In this case, due to the perturbation of high order modes, the linear mode coupling occurs and influences the resonance spectrum. In the study of soliton generation, it is found that avoided mode crossings induced by linear mode coupling can prevent optical soliton formation when affecting resonator modes close to the pump laser frequency [19, 20]. On the other hand, by introducing artificial mode crossing, the anomalous group velocity can also be achieved [21]. Even though the phenomena mentioned in these works are classical, but in the term of phase matching condition, the physics is similar.

In the following research, the mode crossings found in our devices not only change the spectrum transmission, but also leads to failure of evaluating the dispersion properties.

Chapter 4

Device fabrication of silicon nitride ring resonators

Different from fabrication of silicon photonic devices based silicon-on-insulator (SOI) wafers, which is CMOS-compatible and widely used in the laboratory and semiconductor industry, to fabricate integrated silicon nitride device, in particular high Q -factor ring resonators realizing four wave mixing, is still challenging.

Collaborating with Yokoyama Lab in Kyushu University, we perform the subtractive fabrication of silicon nitride ring resonators as well as other optical devices. To discover the diversity of fabrication recipes and compare the material properties, we also design the device layout and order the devices using ligentec process and NTT-AT process.

4.1 SUBTRACTIVE FABRICATION PROCESS

The subtractive process refers to the subtraction of unnecessary parts after the patterning, differing from the lift-off or damascence processes. For optical waveguides, it challenges the etching process to achieve less roughness on the sidewalls. The previous work using similar fabrication processes reported silicon nitride ring resonators with Q -factor up to 5.2×10^4 . The measured loss of waveguides is 2.9 dB/cm [22].

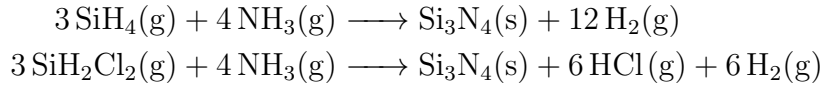
The schematic process flow of the subtractive process is shown in Figure 4.1. First, the silicon dioxide film is deposited on a 4-inch silicon substrate using the TEOS (tetraethyl orthosilicate) source. An alternative method is using a thermal oxidized silicon wafer di-

rectly. The target thickness of silicon dioxide layer is greater than 2 μm to create enough buffer between the silicon nitride film and the silicon substrate. Next is silicon nitride film deposition using chemical vapor deposition methods. Following electron beam (EB) lithography patterning, the silicon nitride layer is etched with inductively coupled plasma reactive-ion etching (ICP RIE) technique. After the resist removal, another layer of silica is cladded. Finally, the chip is cut to couple the light from the edge.

The details of each step will be expanded in the following contents.

4.1.1 Film deposition

Low pressure CVD (LP-CVD) is a traditional method to deposit silicon nitride from the vapor source by the decomposition of chemicals on the surface. Stoichiometric silicon nitride can be obtained by controlling and optimizing the ratio of silicon and nitrogen sources. The precursor of silicon is usually silane (SiH_4) or chloride silane gases, such as dichlorosilane (DCS, SiH_2Cl_2). And the ammonia gas (NH_3) plays the role of nitrogen source.



Considering the toxic gases used in LP-CVD, an alternative approach is to use modern plasma-enhanced CVD (PE-CVD) with liquid source, which has faster growing rate and lower reaction temperature.

To compare the CVD method dependence of film properties, especially the refractive index, in our research, three different CVD facilities—LP-CVD, PE-CVD and liquid source CVD (LS-CVD) are exploited with three different recipes to deposit the silicon nitride films.

Compared with commercial silicon nitride on insulator wafers deposited using LP-CVD, the details of PE-CVD and LS-CVD recipes are listed in Table 4.1. It is apparent from the data that LS-CVD has the fastest rate 23 nm/min, and lowest reaction temperature. In addition, during our experiments, although the flow rate of SN-2 source changes the film growing rate, it does not effect the film stoichiometry and optical properties. It is also worth to mention that all the wafer deposited with above three recipes shows no cracks during the fabrication, suggesting low tensile in silicon nitride films.

4.1.2 Material properties

Fourier-transform infrared spectroscopy

The vast majority of studies on silicon nitride fabrication processes have found that the hydrogen remaining in the films leads to N-H and Si-H bonds, which causes the optical absorption at S and C band [23, 24]. To quantitatively clarify these bonds in our film, we perform the Fourier-transform infrared spectroscopy (FTIR) on the top of silicon nitride film.

The measurement is carried out using attenuated total reflection (ATR) method with SHIMADZU ?. In Figure 4.2, the absorbance is taken from the difference with background transmittance. It can be seen that except the peak around 800 cm^{-1} referring to Si-N stretching mode, two other peaks are located around 2150 and 3350 cm^{-1} , corresponding to Si-H and N-H bonds respectively.

Interestingly, there are also two peaks found at 1020 and 1120 , indicating Si-O symmetric and asymmetric stretching modes. This result may be explained by the fact that in ATR method, the depth of penetration at this wavelength is less than 1 micron, while the thickness of silicon nitride layers in our experiment is targeted at 800 nm .

In conclusion, even though the ammonia free recipe is used in LS-CVD method, the film is still hydrogenated while LP-CVD commercial wafers show least N-H absorbance.

Ellipsometry

4.1.3 Patterning

The sample used in our experiments are usually in the size of $20\text{ mm} \times 20\text{ mm}$, diced off from a 4-inch wafer. Before the electron beam lithography, electron beam resist is spin-coated on the surface of silicon nitride films after several times of cleaning.

But first, a layer of an adhesion promoter, hexamethyldisilazane (HDMS) is coated at 2000 rpm and then baked at $120\text{ }^{\circ}\text{C}$ for 1 min . Next, the positive resist (AR-P 6500, ALLRESIST GmbH) is coated at 1000 rpm and soft-baked at $120\text{ }^{\circ}\text{C}$ for 2 min . The final thickness of resist is around 800 nm to achieve enough thickness during the etching process. The main EB machine used in our experiments is ELIONIX ELS-F100 and the beam dose is 3 nA , 0.6 sec/dot . This

recipe is fully optimized and has small feature sizes and high accuracy around 10 nm. After the lithography, the sample is developed using *o*-xylene.

4.1.4 ICP etching

In order to etch the waveguide layer selectively, ICP-RIE (RIE-400iPB, SAMCO Inc.) is used to remove the unmasked section in silicon nitride layer.

Different from previous work [6], the ICP-RIE facility used in this study is optimized for deep silicon etching. In the key etching step of our recipe, only CHF_3 gas, 6 sccm, is used along with argon gas to clean any residual organic matter over the surface. ICP power is set 50 W, and RF bias power is 20 W.

The etching rate of three kinds of film is listed in Table 4.1. From the data, we can see LS-CVD deposited film has the best selectivity, much higher than LP- and PE-CVD samples. It seems possible that the film density varies from the CVD methods, due to LS-CVD has the fastest growth rate and lowest reaction temperature.

4.1.5 Top-cladding and annealing

The final step is cladding another layer of silicon dioxide. The recipe is as same as the buried oxide layer, using TEOS source. To remove the residual hydrogen in silicon nitride film, an optional step of annealing is necessary.

Traditionally, annealing process can be performed in different cases, after or during CVD deposition [25], after dry etching or after top cladding [26]. Since the first case requires tensile control during cycled deposition-annealing operation [25], in our experiments, annealing before or after top cladding of negatively patterned LS-CVD and PE-CVD sample are merely compared.

To achieve high vacuum during the annealing, we use a tube-type electric furnace. In a high vacuum, the furnace is set first heating from room temperature to 300 °C for 1 h, then heating to 1000 °C for 3 h, keeping at 1000 °C for 4 h, and cooling down to 300 °C for 5 h, then naturally cooling to room temperature.

Shown in Figure 4.4, there are cracks on both the LS-CVD and PE-CVD samples. In contrast, the negatively patterned samples are free of any cracks but is severely contaminated, which possibly

results from the contamination in the tube furnace. In general, the finding of cracks on the top clad layer shows despite the tensile control over the silicon nitride film, even negative EB resist is used for transferring the structure, it is still difficult to annealing the typical TEOS cladded samples with the PE-CVD facility in our fabrication condition.

4.1.6 Edge coupling and chip dicing

In previous works [27], both grating coupling and edge coupling were designed and studied. In this research, considering the broadband frequency conversion motivation, the edge coupling is preferred due to the broader 3 dB bandwidth.

To achieve high coupling efficiency, we adopt monolithic inversed tapered waveguide as the mode convertor. The input and output ports of waveguide are both tapered from normal width $1.5\ \mu\text{m}$ to a narrower end. By FDTD methods, the mode field is swept with different taper end widths.

From the result shown in Figure 4.5a, the mode fields expand horizontally as the taper end width increases proportionally. The largest mode size of $3.4\ \mu\text{m} \times 3.4\ \mu\text{m}$ is successfully demonstrated, but the enhancement is not significant compared with no tapered port in Figure 4.5e. In result, a lensed fiber with spot diameter from $3.0\ \mu\text{m}$ to $3.4\ \mu\text{m}$ is recommended.

In order to precisely define the input and output ports, the chip dicing is required. Compared with conventional mechanical dicing, the laser dicing technique is advantageous at high precision and less damages on the chip edges. The image of laser diced edge is compared with the manually diced one in Figure 4.6. Apparently, the chip using laser dicing has smoother edge, which is helpful to reduce the backward scattering.

4.2 FABLESS SAMPLES VIA FOUNDRIES

Fabless photonic research is becoming a trend for its cheaper and easier external run [28]. There are several foundries all around the world offering the multi-project run service on integrated photonics and quantum optics applications, such as AMF in Singapore, Ligentec in Switzerland, Lionix in Netherlands and etc.

Based on the silicon nitride platform, two independent foundries are evaluated in the following sections in the term of device performance and fabrication techniques.

4.2.1 Ligentec technique

Photonic damascene process [29, 30] used in Ligentec samples improves the waveguide sidewall roughness by depositing the silicon nitride film into the etched thermal oxidized silica. By additive chemical mechanical planarization (CMP), the top surface of silicon nitride is also flatten.

The laser microscope images is shown in . Several layers of different structures are found hierarchically, including the cross pattern stopping the crack during annealing and CMP, the silicon waveguides and a top unknown metallic layer.

4.2.2 NTT-AT technique

NTT-AT technique adopts a different physical vapor method–reactive sputtering to deposit non-hydrogen silicon nitride. Compared with standard silicon sputtering, the nitrogen flow is supplied and reacts with silicon vapor into the silicon nitride film.

Chapter 5

Dispersion evaluation from transmission spectroscopy

5.1 METHODS

5.2 SETUPS

5.3 RESULTS

5.3.1 Device transmission

5.3.2 Dispersion

Chapter 6

Broadband Photon pair generation

6.1 JOINT SPECTRUM INTENSITY

6.2 COINCIDENCE COUNTS VS. PUMP

Chapter 7

Towards intermodal and intramodal photon pair

7.1 SPONTANEOUS FOUR WAVE MIXING

7.2 STIMULATED FOUR WAVE MIXING

Chapter 8

Summary

Acknowledgements

Nam dui ligula, fringilla a, euismod sodales, sollicitudin vel, wisi. Morbi auctor lorem non justo. Nam lacus libero, pretium at, lobortis vitae, ultricies et, tellus. Donec aliquet, tortor sed accumsan bibendum, erat ligula aliquet magna, vitae ornare odio metus a mi. Morbi ac orci et nisl hendrerit mollis. Suspendisse ut massa. Cras nec ante. Pellentesque a nulla. Cum sociis natoque penatibus et magnis dis parturient montes, nascetur ridiculus mus. Aliquam tincidunt urna. Nulla ullamcorper vestibulum turpis. Pellentesque cursus luctus mauris.

Nulla malesuada porttitor diam. Donec felis erat, congue non, volutpat at, tincidunt tristique, libero. Vivamus viverra fermentum felis. Donec nonummy pellentesque ante. Phasellus adipiscing semper elit. Proin fermentum massa ac quam. Sed diam turpis, molestie vitae, placerat a, molestie nec, leo. Maecenas lacinia. Nam ipsum ligula, eleifend at, accumsan nec, suscipit a, ipsum. Morbi blandit ligula feugiat magna. Nunc eleifend consequat lorem. Sed lacinia nulla vitae enim. Pellentesque tincidunt purus vel magna. Integer non enim. Praesent euismod nunc eu purus. Donec bibendum quam in tellus. Nullam cursus pulvinar lectus. Donec et mi. Nam vulputate metus eu enim. Vestibulum pellentesque felis eu massa.

Quisque ullamcorper placerat ipsum. Cras nibh. Morbi vel justo vitae lacus tincidunt ultrices. Lorem ipsum dolor sit amet, consectetur adipiscing elit. In hac habitasse platea dictumst. Integer tempus convallis augue. Etiam facilisis. Nunc elementum fermentum wisi. Aenean placerat. Ut imperdiet, enim sed gravida sollicitudin, felis odio placerat quam, ac pulvinar elit purus eget enim. Nunc vitae tortor. Proin tempus nibh sit amet nisl. Vivamus quis tortor vitae risus porta vehicula.

References

1. Wengerowsky, S., Joshi, S. K., Steinlechner, F., Hübner, H. & Ursin, R. An entanglement-based wavelength-multiplexed quantum communication network. *Nature* **564**, 225–228 (2018).
2. Tchebotareva, A. *et al.* Entanglement between a Diamond Spin Qubit and a Photonic Time-Bin Qubit at Telecom Wavelength. *Phys. Rev. Lett.* **123**, 063601 (2019).
3. Okano, M. *et al.* 0.54 μm Resolution Two-Photon Interference With Dispersion Cancellation for Quantum Optical Coherence Tomography. *Sci. Rep.* **5**, 1–8 (2015).
4. Lu, X., Jiang, W. C., Zhang, J. & Lin, Q. Biphoton Statistics of Quantum Light Generated on a Silicon Chip. *ACS Photonics* **3**, 1626–1636 (2016).
5. Bogaerts, W. *et al.* Silicon microring resonators. *Laser Photonics Rev.* **6**, 47–73 (2012).
6. Ono, Y. *A study of photon-pair generation using silicon nitride ring resonators* Master Thesis (Kyoto University, 2017).
7. Pfeiffer, M. H., Liu, J., Geiselmann, M. & Kippenberg, T. J. Coupling Ideality of Integrated Planar High-Q Microresonators. *Phys. Rev. Appl.* **7**, 1–8 (2017).
8. Leuthold, J., Koos, C. & Freude, W. Nonlinear silicon photonics. *Nat. Photonics* **4**, 535–544 (2010).
9. Agrawal, G. in *Nonlinear Fiber Optics (Fifth Edition)* (ed Agrawal, G.) Fifth Edition, 397–456 (Academic Press, Boston, 2013).
10. Brasch, V. *et al.* Photonic chip-based optical frequency comb using soliton Cherenkov radiation. *Science* (80-.). **351**, 357–360 (2016).

11. Luke, K., Okawachi, Y., Lamont, M. R. E., Gaeta, A. L. & Lipson, M. Broadband mid-infrared frequency comb generation in a Si₃N₄ microresonator. *Opt. Lett.* **40**, 4823 (2015).
12. Xu, Q., Almeida, V. R., Panepucci, R. R. & Lipson, M. Experimental demonstration of guiding and confining light in nanometer-size low-refractive-index material. *Opt. Lett.* **29**, 1626 (2004).
13. Almeida, V. R., Xu, Q., Barrios, C. A. & Lipson, M. Guiding and confining light in void nanostructure. *Opt. Lett.* **29**, 1209 (2004).
14. Mas, S., Caraquitená, J., Galán, J. V., Sanchis, P. & Martí, J. Tailoring the dispersion behavior of silicon nanophotonic slot waveguides. *Opt. Express* **18**, 20839 (2010).
15. Zhang, L., Yue, Y., Beausoleil, R. G. & Willner, A. E. Flattened dispersion in silicon slot waveguides. *Opt. Express* **18**, 20529 (2010).
16. Zhu, M. *et al.* Ultrabroadband flat dispersion tailoring of dual-slot silicon waveguides. *Opt. Express* **20**, 15899 (2012).
17. Nolte, P. W., Bohley, C. & Schilling, J. Tuning of zero group velocity dispersion in infiltrated vertical silicon slot waveguides. *Opt. Express* **21**, 1741 (2013).
18. Zhang, L. *et al.* Generation of two-cycle pulses and octave-spanning frequency combs in a dispersion-flattened microresonator. *Opt. Lett.* **38**, 5122 (2013).
19. Herr, T. *et al.* Mode spectrum and temporal soliton formation in optical microresonators. *Phys. Rev. Lett.* **113**, 1–6 (2014).
20. Bao, C. *et al.* Deterministic single soliton generation via mode-interaction in microresonators. **4**, SW4M.2 (2018).
21. Kim, S. *et al.* Dispersion engineering and frequency comb generation in thin silicon nitride concentric microresonators. *Nat. Commun.* **8** (2017).
22. Cheng, X., Hong, J., Spring, A. M. & Yokoyama, S. Fabrication of a high-Q factor ring resonator using LSCVD deposited Si₃N₄ film. *Opt. Mater. Express* **7**, 2182 (2017).
23. Ay, F. & Aydinli, A. Comparative investigation of hydrogen bonding in silicon based PECVD grown dielectrics for optical waveguides. *Opt. Mater. (Amst)*. **26**, 33–46 (2004).

24. Agnihotri, O. P. *et al.* Advances in low temperature processing of silicon nitride based dielectrics and their applications in surface passivation and integrated optical devices. *Semicond. Sci. Technol.* **15** (2000).
25. Luke, K., Poitras, C. B. & Lipson, M. Overcoming SiN film stress limitations for high quality factor ring resonators. *2013 IEEE Photonics Soc. Summer Top. Meet. Ser. PSSTMS 2013* **21**, 64–65 (2013).
26. Wang, L. *et al.* Nonlinear silicon nitride waveguides based on PECVD deposition platform. *Opt. Express* **26**, 9645 (2018).
27. Sunada, Y. *Measurement of Group Velocity Dispersion of Silicon Nitride Ring Resonators toward Photon-pair Generation* Bachelor Thesis (Kyoto University, 2018).
28. Hochberg, M. & Baehr-Jones, T. Towards fabless silicon photonics. *Nat. Photonics* **4**, 492–494 (2010).
29. Pfeiffer, M. H. P. *et al.* Photonic Damascene process for integrated high-Q microresonator based nonlinear photonics. *Optica* **3**, 20 (2016).
30. Pfeiffer, M. H. P. *et al.* Photonic damascene process for low-loss, high-confinement silicon nitride waveguides. *IEEE J. Sel. Top. Quantum Electron.* **24**, 1–11 (2018).

List of Figures

2.1	Planar waveguide	33
2.2	An all-pass type ring resonator	33
2.3	The transmission spectrum of a ring resonator	33
2.4	Illustration of wavelength transmission spectrum of ring resonators	34
2.5	Illustration of possible energy diagram in typical third-order nonlinear processes	34
3.1	Refractive index and dispersion parameter measured in reference	35
3.2	Waveguide dispersion map simulated by Lumerical MODE	35
3.3	Illustration of a double vertical slot waveguide	36
3.4	Modes of the double vertical slot waveguide	36
3.5	Modes of the double vertical slot waveguide	37
4.1	Schematic process flow of the subtractive process	37
4.2	Caption	38
4.3	Elliposometry	38
4.4	Laser microscope images of samples after annealing process	39
4.5	Mode field at the taper end	40
4.6	Caption	40
4.7	Laser microscope images of Ligentec smaples	41

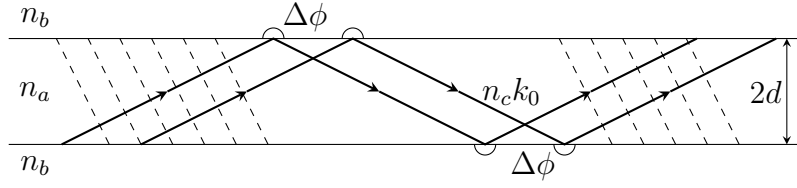


Figure 2.1: **Planar waveguide.** The upper and bottom layer are cladding and the middle is core layer. $\Delta\phi$ represents the Goos-Hänchen shift at the boundary.

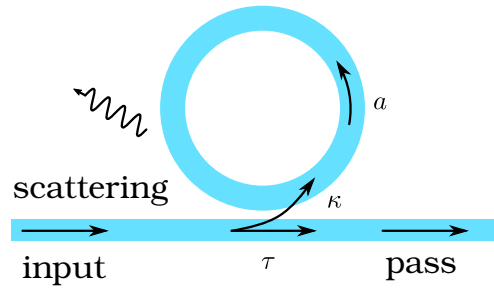


Figure 2.2: **An all-pass type ring resonator.** The transmitted spectrum is filtered periodically by the ring waveguide, in the case satisfying resonance condition.

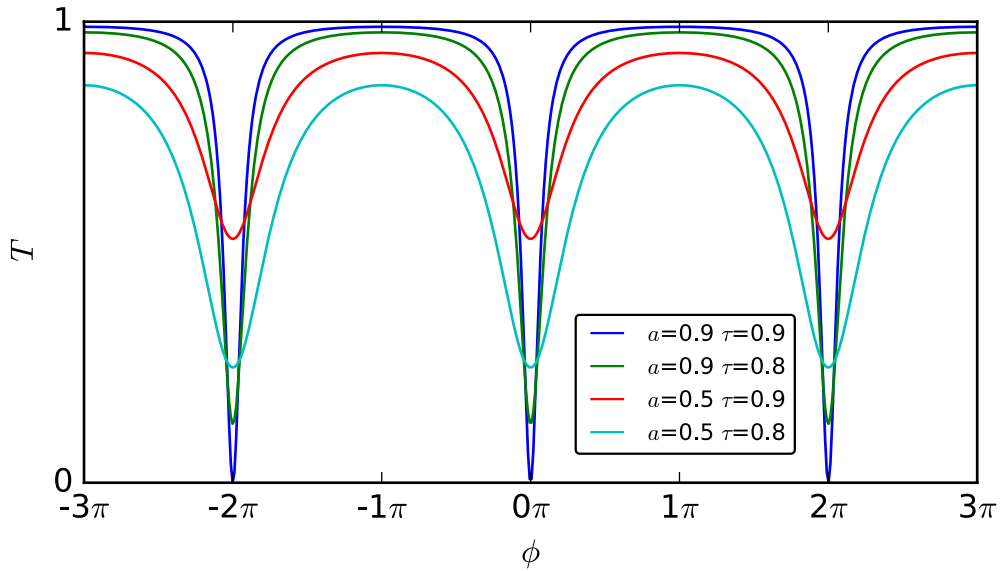


Figure 2.3: **The transmission spectrum of a ring resonator.**

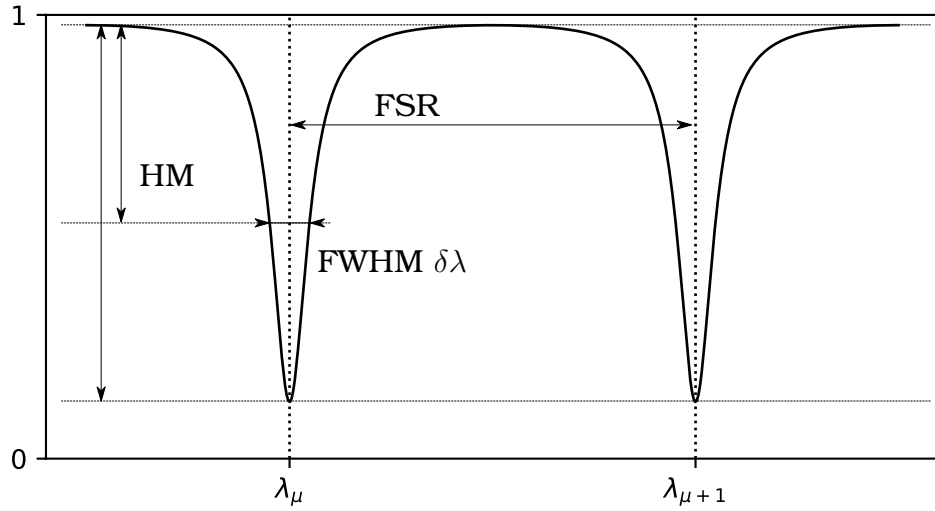


Figure 2.4: **Illustration of wavelength transmission spectrum of ring resonators.** FSR, free spectral range, the distance between neighbouring resonant wavelength. FWHM, full width at half maximum.

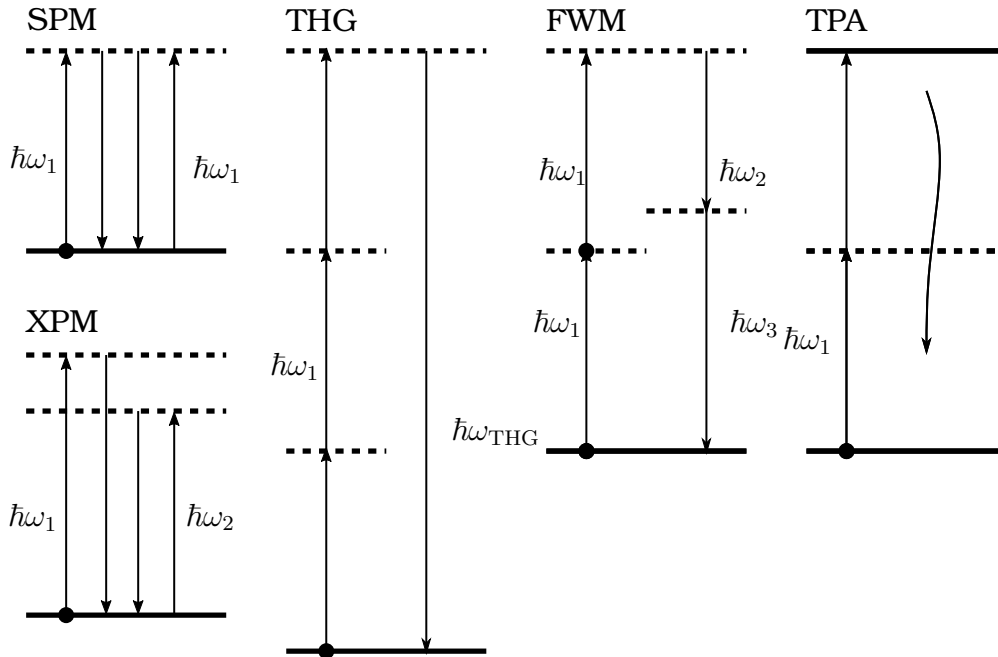


Figure 2.5: **Illustration of possible energy diagram in typical third-order nonlinear processes.**

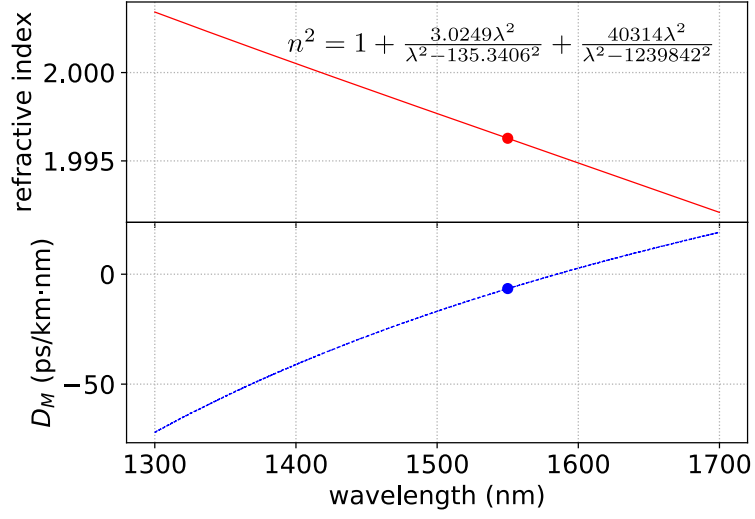


Figure 3.1: **Refractive index and dispersion parameter measured in reference.** $\lambda=1550$ nm, $n=1.9963$ and $D_M = -6.5656$ ps/(km nm).

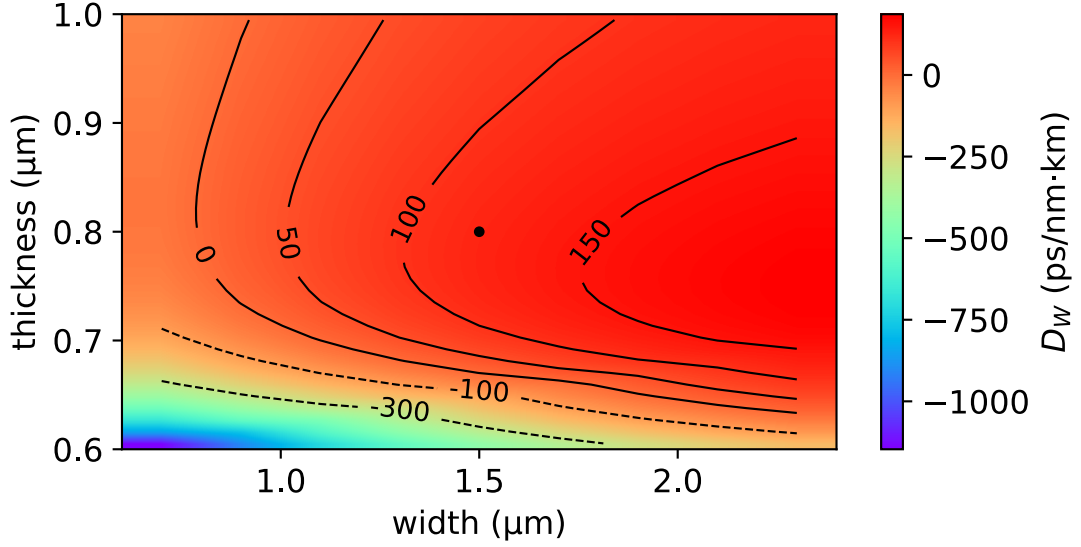


Figure 3.2: **Waveguide dispersion map simulated by Lumerical MODE.** The central wavelength to perform the simulation is 1550 nm and the precision is nm. We select the fundamental TE mode as the objective to study the waveguide dispersion. The scattered point in the figure is 1.5- μm -wide and 0.8- μm -thick.

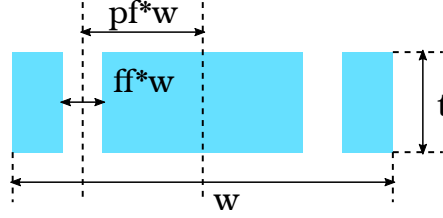


Figure 3.3: **Illustration of a double vertical slot waveguide.** The cyan region is Si_3N_4 waveguide and surrounded by silica.

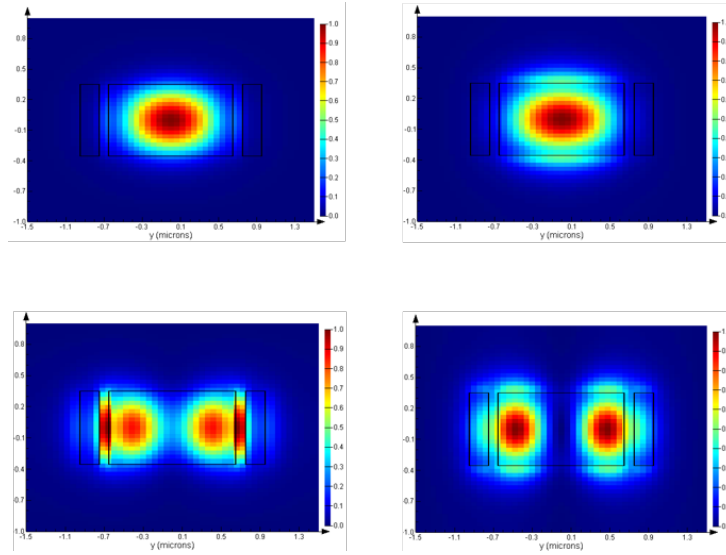


Figure 3.4: **Modes of the double vertical slot waveguide.**

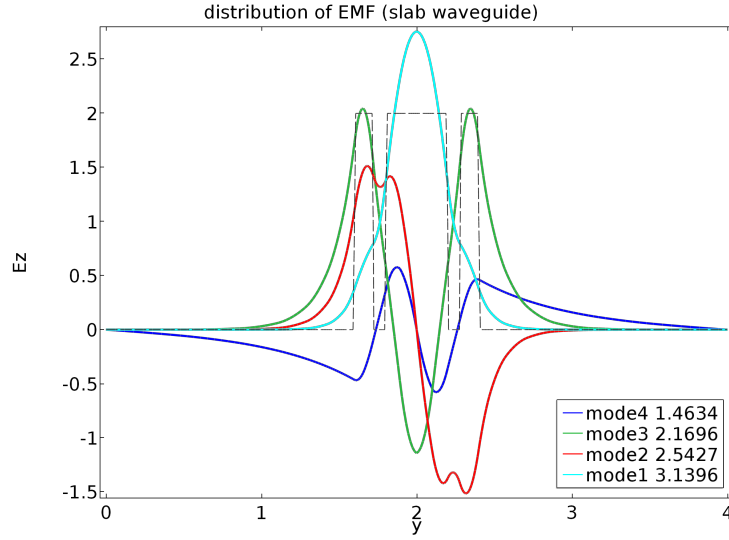


Figure 3.5: **Modes of the double vertical slot waveguide.**

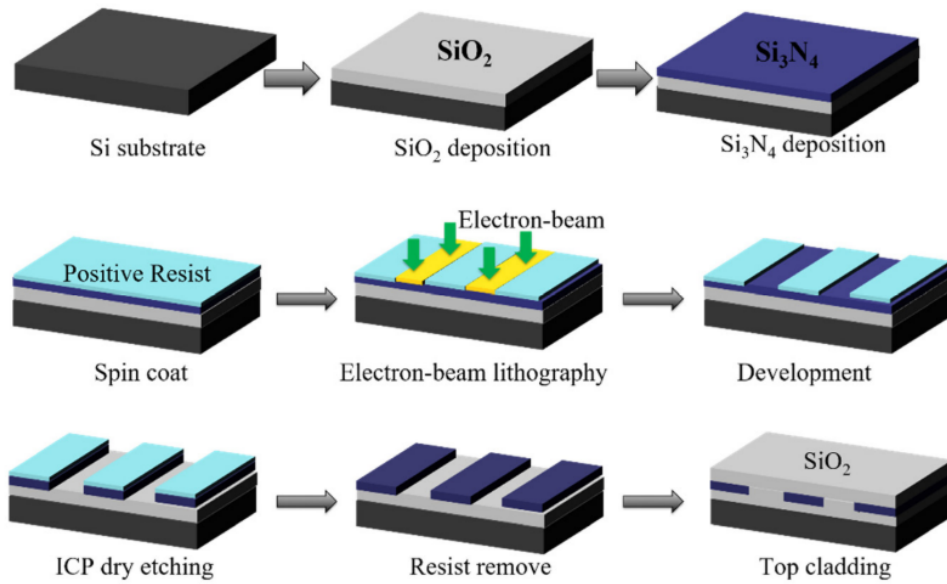


Figure 4.1: **Schematic process flow of the subtractive process.**

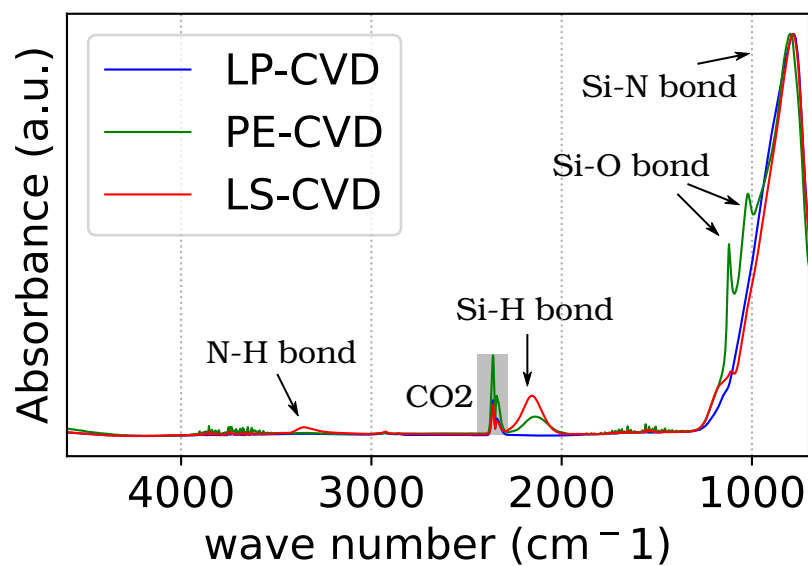


Figure 4.2: Caption

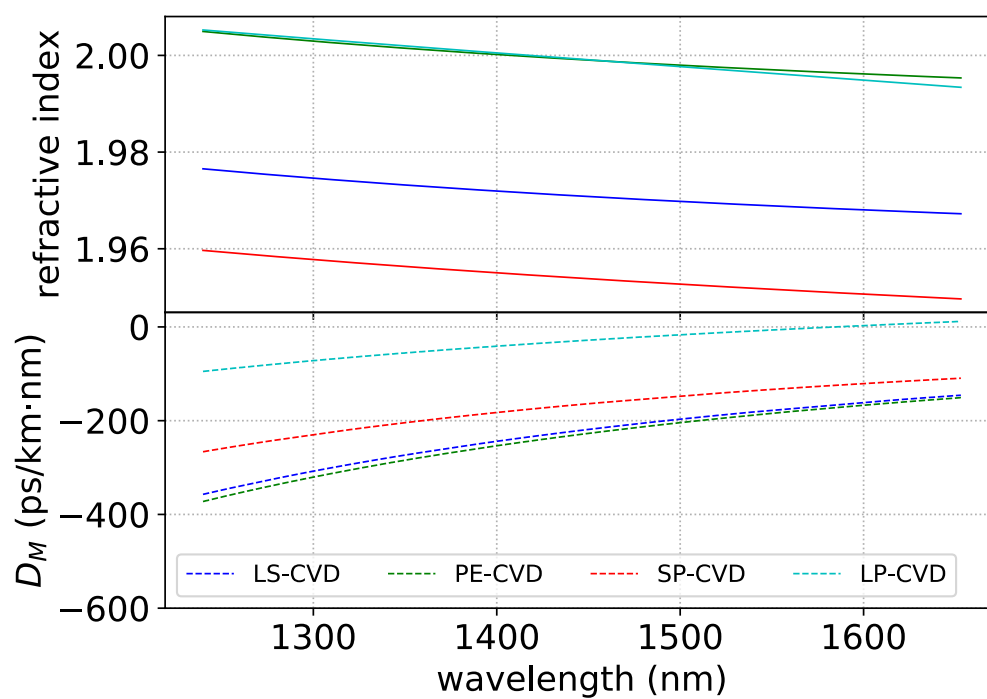


Figure 4.3: **Ellipsometry.**

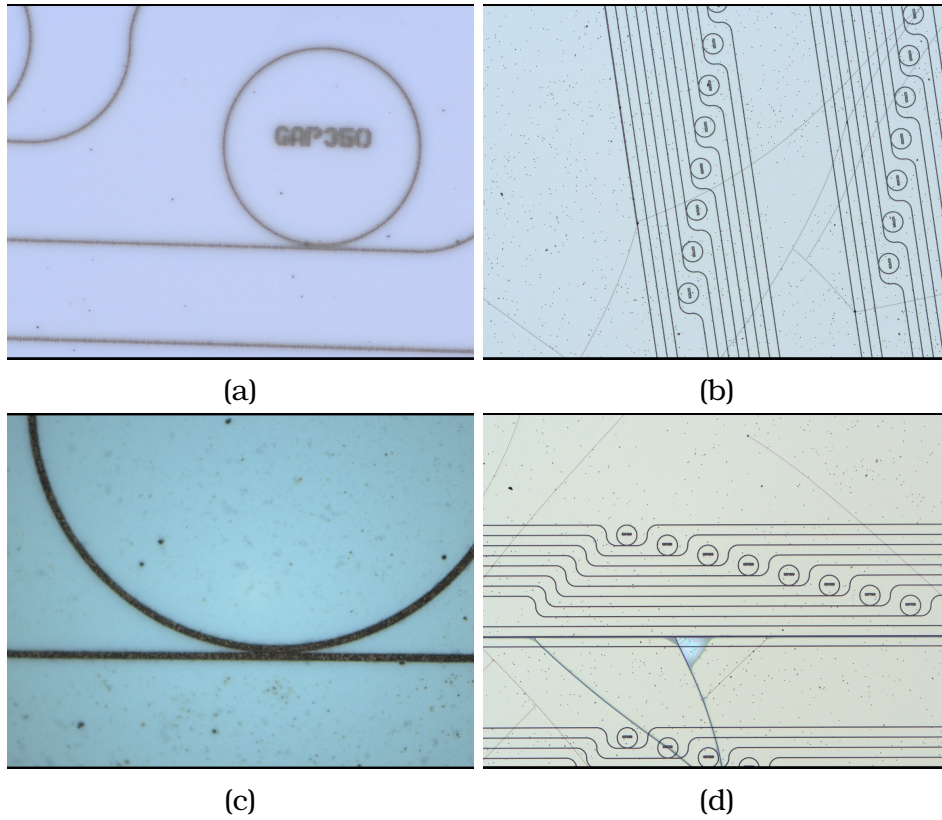


Figure 4.4: **Laser microscope images of samples after annealing process.** All the sample are annealed under the same circumstance. **a.** LS-CVD sample without top cladding. **b.** LS-CVD sample with TEOS top-cladding. **c.** PE-CVD sampele without top cladding. **d.** PE-CVD sample with TEOS top-cladding.

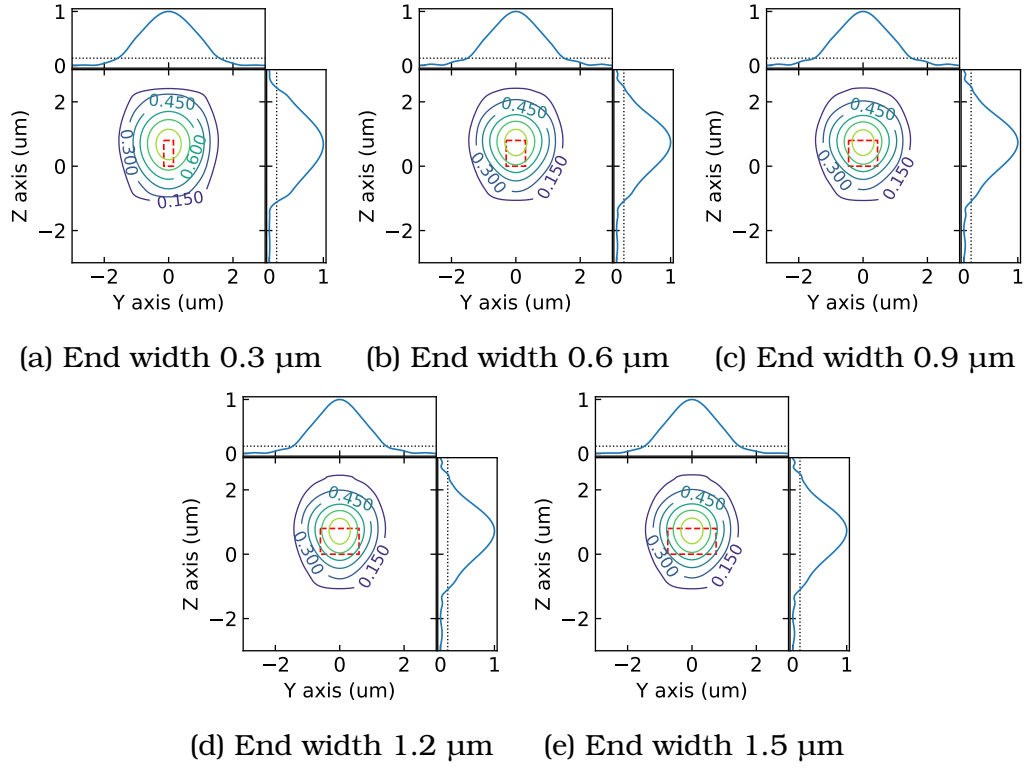


Figure 4.5: **Mode field at the taper end.** The outline of taper edge is profiled.

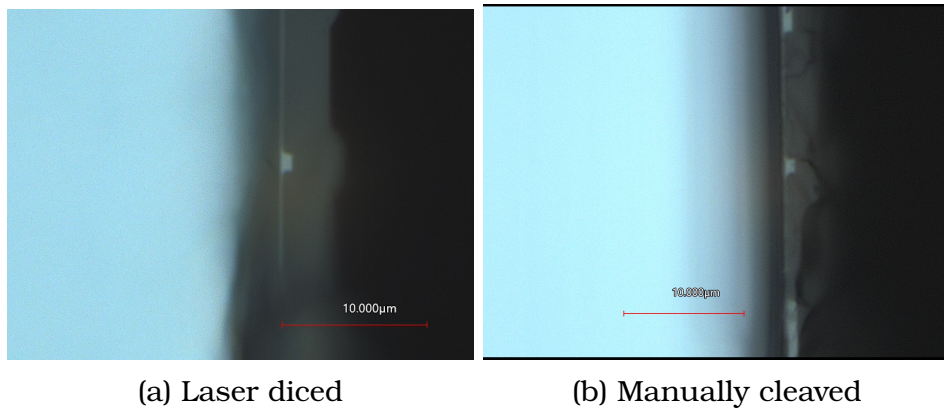


Figure 4.6: **Caption.**

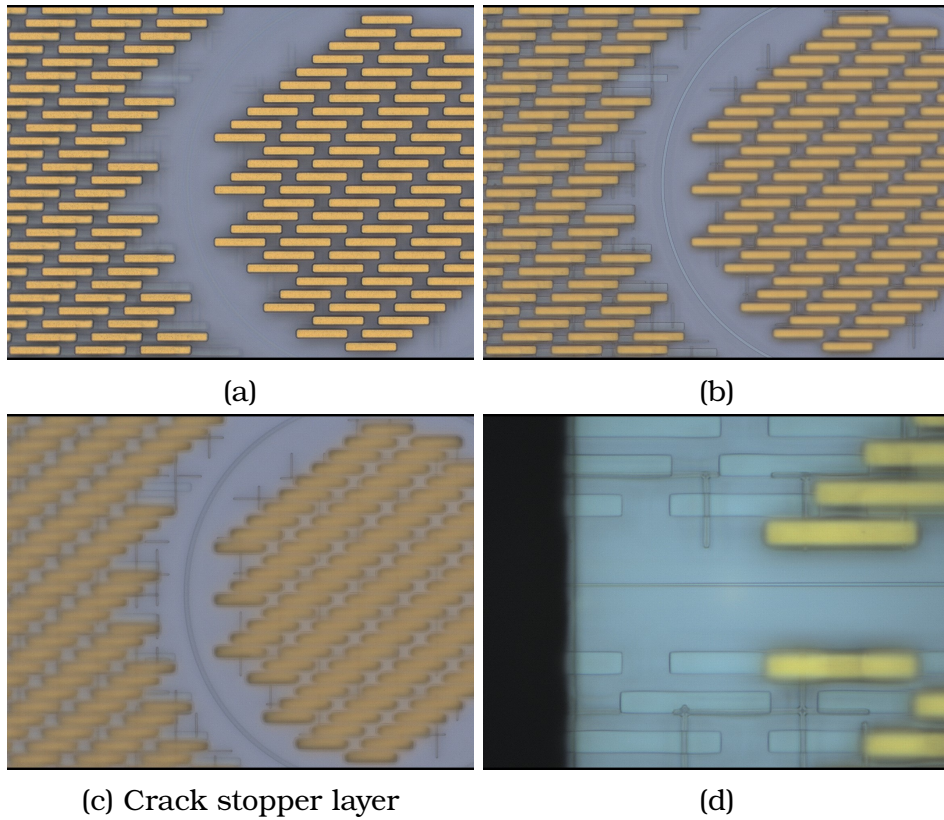


Figure 4.7: **Laser microscope images of Ligentec samples.** By lowering the focus depth, three layers are observed. **a.** Top metallic layer. **b.** Device layer. **c.** Crack stopper layer. **d.** Mode convertor

List of Tables

4.1	Recipes of CVD methods used in this research	43
4.2	Etching rate and selectivity of ICP process	43

	LP-CVD	PE-CVD	LS-CVD
Facility	-	SAMCO PD-220NL	SMACO PD-100ST
Source	DCS:NH ₃ :N ₂	SiH ₄ :NH ₃ :N ₂ =6:5:189 sccm	SN-2:N ₂ =0.5:30 sccm
Chamber Temp.	750°C-800°C	upper 150°C lower 350°C	upper 150°C lower 180°C
RF Power	-	40 W	30 W
Deposition Rate	-	15 nm/min	23 nm/min

Table 4.1: **Recipes of CVD methods used in this research.** In the case of PE-CVD and LS-CVD, upper electrode and lower electrode are set at different temperature. RF power refers to radio frequency power used to excite the precursor gasses.

	Film Etching Rate (nm/min)	Resist Etching Rate (nm/min)	Selectivity
LP-CVD	19.20	12.76	1.50
PE-CVD	23.48	14.29	1.64
LS-CVD	27.40	2.08	13.17

Table 4.2: **Etching rate and selectivity of ICP process.**

Appendix A

Dispersion simulation

Appendix B

Layout design

Appendix C

Process